PHYSICAL REVIEW B **102**, 174442 (2020)

In-plane spin-orbit torque magnetization switching and its detection using the spin rectification effect at subgigahertz frequencies

Motomi Aoki,[1] Ei Shigematsu,[1] Masayuki Matsushima,[1] Ryo Ohshima,[1] Syuta Honda,[2] Teruya Shinjo,[1]
Masashi Shiraishi,[1] and Yuichiro Ando[1,*]
[1] *Department of Electronic Science and Engineering, Kyoto University, Kyoto, Kyoto 615-8510, Japan*
[2] *Department of Pure and Applied Physics, Kansai University, Suita, Osaka 564-8680, Japan*

(Received 29 August 2020; revised 5 November 2020; accepted 5 November 2020; published 30 November 2020)

In-plane magnetization reversal of a permalloy/platinum bilayer was detected using the spin rectification effect. Using a subgigahertz microwave frequency to excite spin-torque ferromagnetic resonance (ST-FMR) in the bilayer induces two discrete DC voltages around an external static magnetic field of 0 mT. These discrete voltages depend on the magnetization directions of the permalloy and enable detection of the in-plane magnetization reversal. The threshold current density for the magnetization reversal is around 10–20 $\mathrm{MA/cm^2}$, the same order as for known spin-orbit torque switching with in-plane magnetization materials. The magnitude of the signal is the same or larger than that of the typical ST-FMR signal; that is, detection of magnetization switching is highly sensitive in spite of deviation from the optimal ST-FMR condition. The proposed method is applicable to a simple device structure even for a small ferromagnetic electrode with a width of 100 nm.

DOI: 10.1103/PhysRevB.102.174442

I. INTRODUCTION

Magnetization switching using spin-orbit torque (SOT) [1–7] has attracted much research interest because it enables fast, low-power, and high-endurance write operations in nonvolatile magnetic memories such as magnetoresistive random access memory. The large spin Hall angle θ_{SHE} of spin-orbit materials makes them essential for highly efficient magnetization switching via SOT. Therefore, quantitative investigations of θ_{SHE} have been conducted on a wide variety of materials including metals [8–14], semiconductors [15–18], topological insulators [19–28], and even light-element materials [29–32]. Spin-torque ferromagnetic resonance (ST-FMR) is one of the main methods for this, where θ_{SHE} is evaluated from the line shape of the DC voltage signals generated by the spin rectification effect (SRE) [33–35]. Typical ST-FMR signals consist of two components, symmetric and antisymmetric Lorentzian functions. In the simplest case, θ_{SHE} is calculated from the ratio of their magnitudes. However, the Oersted field induced by an applied microwave generates both symmetric and antisymmetric components whose magnitudes are sensitive to the phase difference between the Oersted field and the magnetic moment M [34,36–38]. Furthermore, one should consider the contributions of the anomalous Nernst effect (ANE), the spin Seebeck effect, and the inverse spin Hall effect (ISHE) induced by spin pumping [39–41]. The fieldlike torque also generates an antisymmetric component that becomes pronounced when the interfacial Rashba effect is significant. Various approaches have been proposed to distinguish SOT-related FMR signals from unwanted effects. These methods include phase-sensitive detection, comparing different ferromagnetic metals, using signal dependence on the thickness of the ferromagnetic layer, and combining with optical detection [42,43]. However, their procedures for device fabrication, measurement, and analysis are complicated.

Most ST-FMR studies aim to achieve ultrafast and low-power magnetization switching. Therefore, material search using SOT magnetization switching is a determinative method. The device structure for magnetization switching, however, is more complicated than that for ST-FMR, which impedes the search for a wide variety of spin-orbit materials. Magnetization switching in perpendicular magnetization materials can be detected via the anomalous Hall effect (AHE). Confirming magnetization switching in this case needs fabrication of two nonmagnetic electrodes for measuring the Hall voltage of the ferromagnetic electrode whose polarization corresponds to the magnetization direction. Applying the AHE to in-plane magnetization materials is generally difficult. Therefore, additional spin valves such as magnetic tunnel junctions (MTJs) and giant magnetoresistive devices are commonly fabricated [2,44,45]. It is much preferred to detect magnetization switching of a single ferromagnetic layer with a simple device structure.

In this study, we detect in-plane magnetization switching of a single ferromagnetic layer on spin-orbit materials by applying subgigahertz (sub-GHz) microwaves. The method, hereafter called “low-frequency ST-FMR” (LFST-FMR), has the same device structure as that of ST-FMR and does not require fabricating additional electrodes or spin valves. By only applying sub-GHz microwaves to an electrode without a magnetic field, we determine the magnetization direction as the polarity of a DC voltage. Surprisingly, the detection sensitivity is higher than that of ST-FMR. Therefore, magnetization switching can be detected even for a ferromagnetic electrode as small as 100 nm in width, less than one-tenth of

---

[*] ando@kuee.kyoto-u.ac.jp

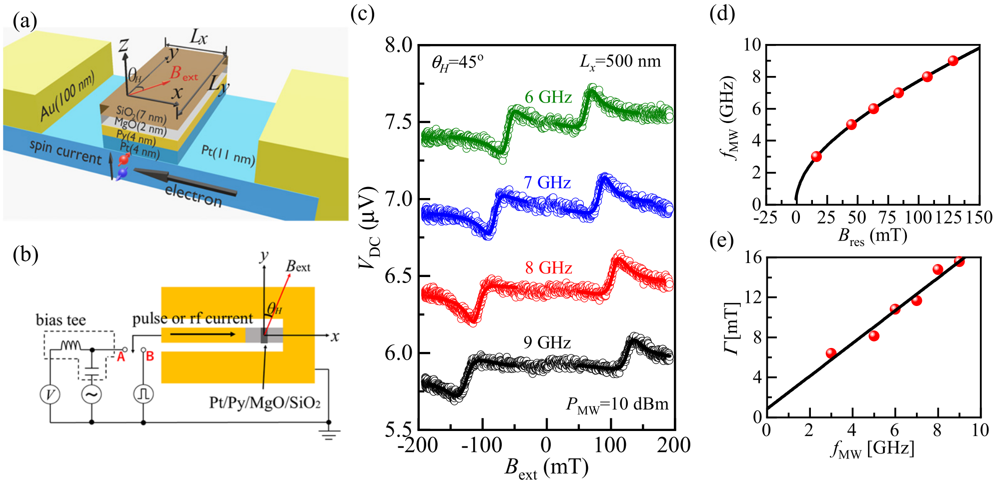

FIG. 1. Schematics of (a) the Py/Pt device and (b) an equivalent electric circuit for demonstrating the magnetization switching induced by spin-orbit torque (SOT). (c) SOT-induced ferromagnetic resonance (ST-FMR) signals for $f_{MW} = 6$, 7, 8, and 9 GHz at $\theta_H = 45°$. Lines are fit using Eq. (1). (d) Relationship between f_{MW} and B_{res}. The dots are experimental data, and the solid line is a fitting curve using Eq. (2). (e) Linewidth of the ST-FMR signals, Γ , obtained by fitting using Eq. (1) as a function of f_{MW}. The dots are experimental data, and the solid line is their linear fitting.

the minimum spatial resolution of optical methods using the magneto Kerr effect [46].

II. SAMPLE FABRICATION AND EXPERIMENTAL PROCEDURE

Figures 1(a) and 1(b) show schematics of the device structure and the equivalent electric circuit in this study. First, Pt(15 nm)/Ni$_{80}$Fe$_{20}$ (Py, 4 nm)/MgO (2 nm) layers were deposited on the MgO(100) substrate using electron-beam lithography and electron-beam deposition. Because the MgO layer has a deliquescent character, a 7-nm-thick SiO$_2$ layer was deposited on the MgO layer by rf magnetron sputtering in different chamber after short-time exposure to the air. Then, a rectangular Py/MgO/SiO$_2$ ferromagnetic electrode was fabricated using electron-beam lithography and argon ion (Ar$^+$) milling. The Ar$^+$ milling was stopped after milling of the 4-nm-thick Pt layer to keep an 11-nm-thick Pt channel. Finally, a Ti (3 nm)/Au (100 nm) coplanar waveguide was fabricated using electron-beam lithography and electron-beam deposition. The length of the Py layer along the y direction, L_y, was varied from 1 to 20 μm and that along the x direction, L_x, was varied from 0.1 to 20 μm. In the ST-FMR studies, a static magnetic field was applied in the film plane with a varying field orientation angle θ_H as shown in Fig. 1(a). (See the Supplemental Material [47].) Microwave radiation with frequency f_{MW} was applied using an analog commercial signal generator (KEYSIGHT N5173B EXG) to excite the FMR of the Py layer, and a DC voltage V_{DC} was measured using a nanovoltmeter (Keithley Nanovoltmeter 2182A). In the magnetization switching study, a function generator (Agilent 33622A) was used to apply a pulse-shaped charge current (pulse current). All the measurements were carried out at room temperature.

Figure 1(c) shows typical ST-FMR signals, i.e., V_{DC} as a function of the external magnetic flux density B_{ext}, at $\theta_H = 45°$ for various values of f_{MW}. The values of L_x and L_y are 500 nm and 20 μm, respectively, one or two orders lower than those of typical ST-FMR measurement devices. The microwave power P_{MW} was 10 dBm. Clear ST-FMR signals were obtained both at positive and negative B_{ext} for up and down sweeps. Whereas similar ST-FMR signals were obtained for $f_{MW} = 6$–9 GHz, the resonance field B_{res} gradually approaches 0 mT with decreasing f_{MW}. The ST-FMR signal $V_{DC}(\theta_M, B_{ext})$ is expressed as

$$V_{DC}(\theta_M, B_{ext}) = \frac{1}{4}\frac{dR}{d\theta_M}\frac{\gamma I_{MW}\sin\theta_M}{\Gamma 2\pi\left(\frac{df_{MW}}{dB_{ext}}\right)\Big|_{B_{ext}=B_{res}}} \times\left(S\frac{\Gamma^2}{\Gamma^2+(B_{ext}-B_{res})^2} + A\frac{\Gamma(B_{ext}-B_{res})}{\Gamma^2+(B_{ext}-B_{res})^2}\right), \qquad (1)$$

where R is the resistance of the Py/Pt device, I_{MW} is the rf current through the microstrip, θ_M is the angle of the magnetization rotation axis from the $+y$ direction as shown in Fig. 1(b), S and A are the coefficients of the symmetric and antisymmetric Lorentzian, respectively, and Γ is the half-width at half maximum of the Lorentzian function. We obtained B_{res} and Γ by fitting Eq. (1). For the in-plane ferromagnetic films, the FMR condition is the Kittel formula [12]:

$$f_{MW} = \frac{\gamma}{2\pi}\sqrt{[B_{res}+(N_X-N_Y)\mu_0 M_s][B_{res}+(N_Z-N_Y)\mu_0 M_s]}, \qquad (2)$$

where M_s is the saturation magnetization; γ is the gyrometric ratio; and N_X, N_Y, and N_Z are the demagnetization factors along the X, Y, and Z axes, respectively. Whereas Z axis is parallel to the z axis, the $Y(X)$ axis is parallel (perpendicular) to the magnetization under application of B_{ext}. The fitting using Eq. (2) is shown in Fig. 1(d), which yields $(N_Z - N_Y)\mu_0 M_s = 0.58 \pm 0.006$ T and $(N_X - N_Y)\mu_0 M_s = 8.9 \times 10^{-4} \pm 5.7 \times 10^{-4}$ T. Because the shape anisotropy equally contributes to N_X and N_Y at $\theta_H = 45°$ and there is almost no crystal anisotropy in the Py layer, N_X and N_Y are expected to show

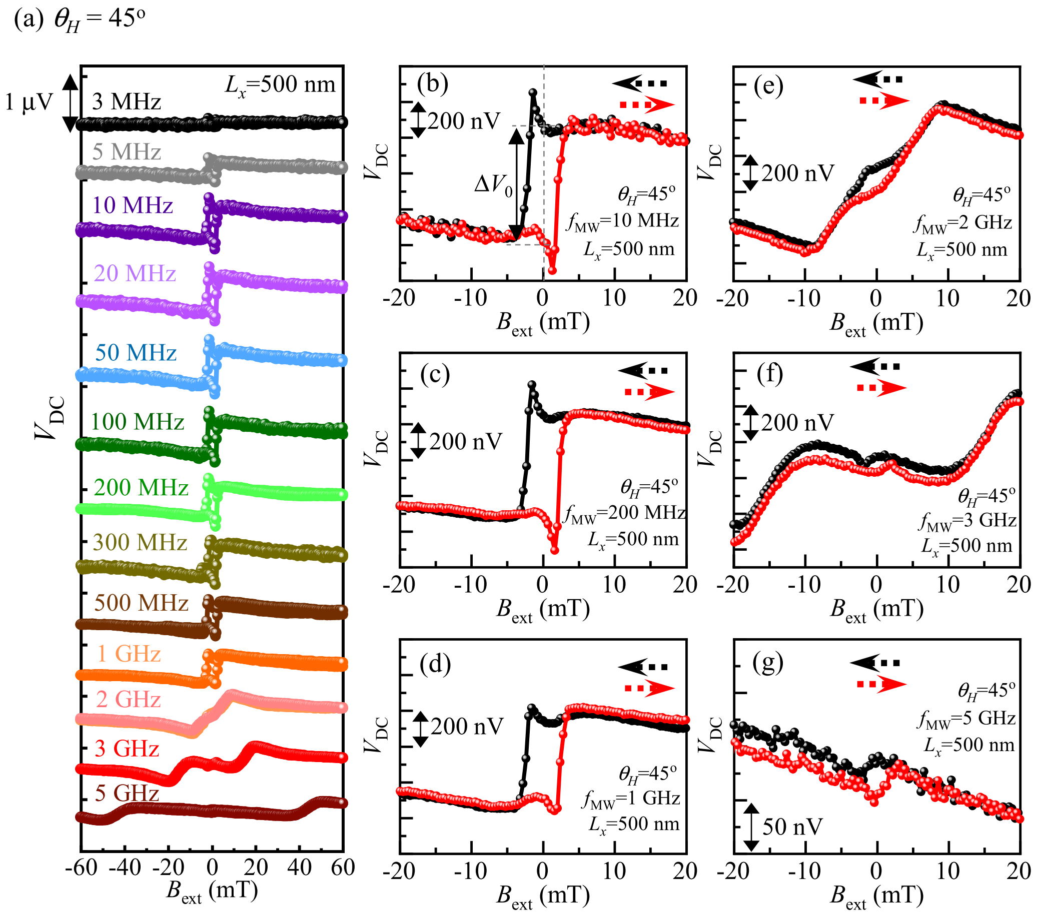

FIG. 2. (a) ST-FMR signals for f_{MW} below 5 GHz at $\theta_H = 45^\circ$. P_{MW} was 10 dBm. (b)–(g) Enlarged ST-FMR signals around $B_{ext} = 0$ mT at f_{MW} = (b) 10 MHz, (c) 200 MHz, (d) 1 GHz, (e) 2 GHz, (f) 3 GHz, and (g) 5 GHz.

the same value. Figure 1(e) shows Γ for the FMR signals as a function of f_{MW}, confirming a linear relationship. The intercept of the Γ axis, caused by nonuniformity of the ferromagnetic layer, is 0.86 ± 1.1 mT. Results of $f_{MW} = 5$ and 3 GHz were also added to Figs. 1(d) and 1(e), spectra of which are shown in Fig. 2(a).

III. SUB-GHz LFST-FMR SIGNALS

Now we focus on the ST-FMR signals at low f_{MW}, namely, LFST-FMR signals. Figure 2(a) shows the ST-FMR signals with various f_{MW} values at $\theta_H = 45^\circ$. For $f_{MW} = 5$ GHz, clear ST-FMR signals similar to those of Fig. 1(c) were obtained around $B_{res} = \pm 45$ mT for both up and down sweeps. B_{res} was decreased by decreasing f_{MW} and finally reached around 0 mT for $f_{MW} \leqslant 2$ GHz, according to the Kittel formula as shown in Fig. 1(e). The signal shapes for up and down sweeps are almost identical for $f_{MW} \geqslant 2$ GHz. In contrast, the field range of the two ST-FMR signals corresponding to positive and negative B_{res} are superimposed on each other for $f_{MW} \leqslant 1$ GHz. Figure 2 shows the enlarged ST-FMR signals around 0 mT at f_{MW} = (b) 10 MHz, (c) 200 MHz, (d) 1 GHz, (e) 2 GHz, (f) 3 GHz, and (g) 5 GHz. For $f_{MW} = 5$ GHz, small hysteresis with a magnitude of 20 nV was obtained around 0 mT. This might be due to the nonresonant SRE or ANE [48,49]. As f_{MW} decreased, the magnitude of the hysteresis increased, and the steep changes in V_{DC} around ±2 mT due to the magnetization switching became pronounced. Here we note that the upper and lower V_{DC} values in the hysteresis correspond to the magnetization directions along the $+y$ and $-y$ directions, respectively. This means that we can detect the magnetization direction by measuring V_{DC} with low-f_{MW} microwaves. The hysteresis was detected even for $f_{MW} < 10$ MHz and came under the detection limit for $f_{MW} < 1$ MHz. It should be noted that magnetization is almost aligned along the y direction around 0 mT because of the shape anisotropy, indicating that the LFST-FMR signals, i.e., the rectangular hysteresis in the $V_{DC} - B_{ext}$ curves, were generated with the magnetization along y. To confirm this, ST-FMR signals were measured at $\theta_H = 0^\circ$, i.e., along y. The results are displayed in Fig. 3. The usual ST-FMR signals at high B_{ext} disappeared for $f_{MW} \geqslant 2$ GHz, which is expected from Eq. (1). In contrast, considerable rectangular LFST-FMR signals were still detected for $f_{MW} < 2$ GHz. The rectangular shapes were slightly modulated from those of $\theta_H = 45^\circ$ because of θ_H-dependent magnetization switching. Figure 4 shows the f_{MW} dependence of the hysteresis magnitude ΔV_0, which is the difference between the upper and lower V_{DC} values of the LFST-FMR signals at $B_{ext} = 0$ mT for $\theta_H = 0^\circ$ and 45°. ΔV_0 shows a maximum around f_{MW} = 50–500 MHz both for $\theta_H = 0^\circ$ and

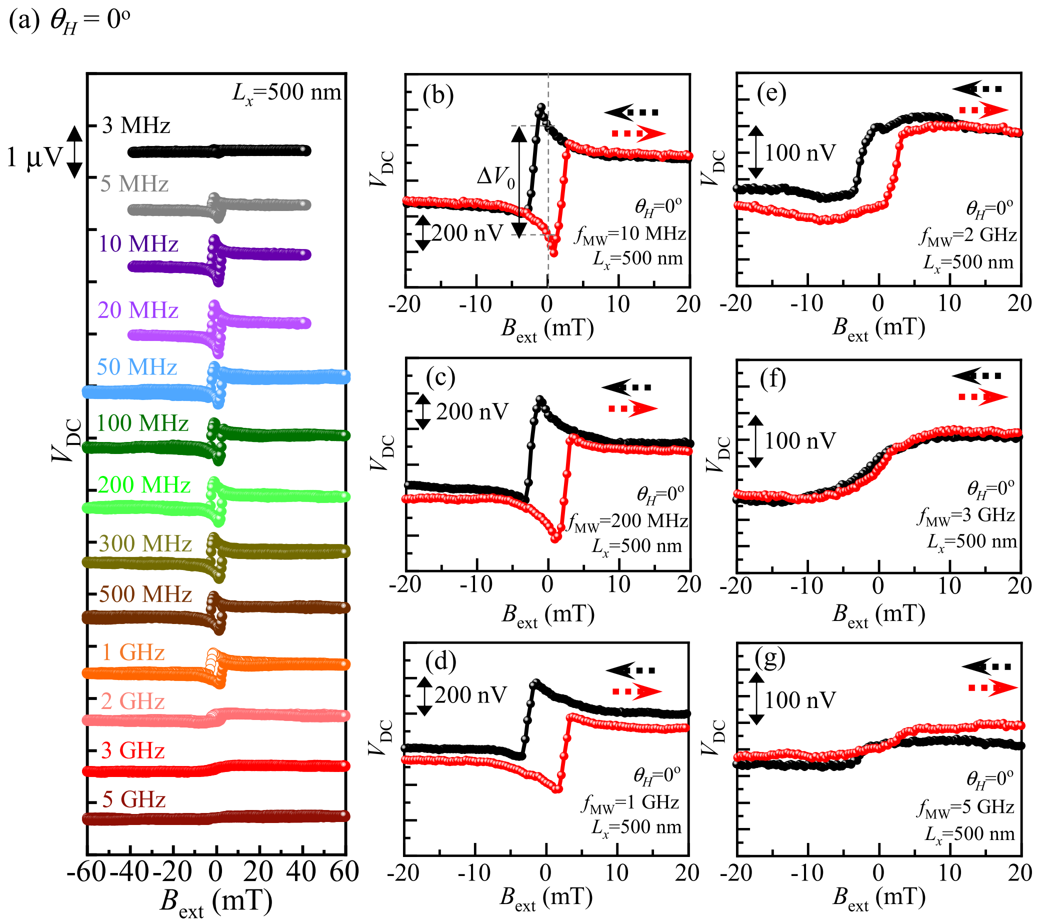

FIG. 3. (a) ST-FMR signals for f_{MW} below 5 GHz at $\theta_H = 0^\circ$. P_{MW} was 10 dBm. (b)–(g) Enlarged ST-FMR signals around $B_{ext} = 0$ mT at $f_{MW} =$ (b) 10 MHz, (c) 200 MHz, (d) 1 GHz, (e) 2 GHz, (f) 3 GHz, and (g) 5 GHz.

45°. One possible origin of the reduction in ΔV_0 below 50 MHz is due to the cutoff frequency (40 MHz) of the bias tee, shown in Fig. 1(b). Surprisingly, ΔV_0 for 50–500 MHz is comparable to or greater than the magnitude of the ST-FMR signals at $\theta_H = 45^\circ$ for $f_{MW} > 3$ GHz. The possible origin of such a large ΔV_0 will be discussed in Sec. V.

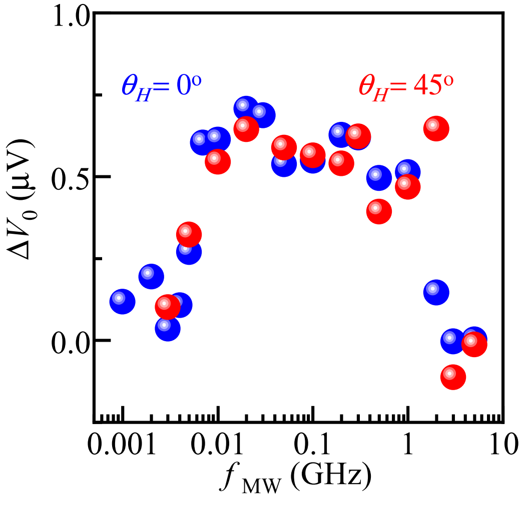

FIG. 4. f_{MW} dependence of the magnitude of the hysteresis signals, ΔV_0, i.e., difference between upper and lower V_{DC} values of the rectangular hysteresis signals at $B_{ext} = 0$ mT for $\theta_H = 0^\circ$ and 45°.

IV. DETECTION OF MAGNETIZATION SWITCHING

We now shift our focus to the main result of this work. Figure 5(a) shows the experimental procedure for demonstrating SOT magnetization switching. First, (1) the magnetization direction was set to the initial direction ($+y$ or $-y$) by applying a sufficient magnetic flux density B_{SET} with $\theta_H = 0^\circ$. Then, (2) B_{SET} was set to 0 mT, and LFST-FMR was used to measure the DC voltage in the initial magnetization direction, V_{DC1}. Then, (3) the circuit switch was changed from A to B to protect the signal generator from the pulse voltage generated by the pulse generator [see Fig. 1(b)]. After the circuit was changed, (4) a pulse voltage was applied under a small magnetic flux density B_{PLS}. Finally, (5) the switch was changed from B to A followed by (6) measuring V_{DC2} at 0 mT to compare with V_{DC1}. The procedure was repeated with a different pulse voltage. Steps (1) and (2) are optional and can be skipped except at the beginning of the measurements. Figure 5(b) shows a hysteresis SOT-switching signal, $\Delta V = (V_{DC2} - V_{DC1})$, as a function of pulse current density J_{PLS} in the Pt layer. L_x, L_y, f_{MW}, and P_{MW} were 500 nm,

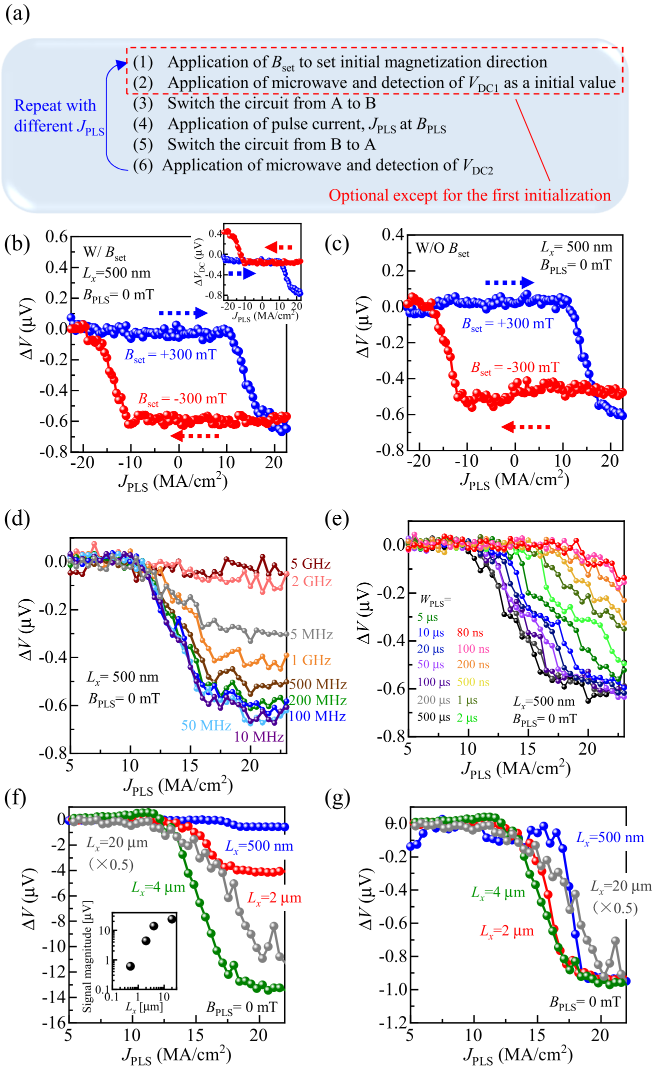

FIG. 5. (a) Procedure for demonstrating SOT magnetization switching. (b) Hysteresis SOT-switching signal, $\Delta V = (V_{DC2} - V_{DC1})$, as a function of pulse charge-current density J_{PLS} at $\theta_H = 0°$. Steps (1)–(3) were carried out for every J_{PLS}. The raw data are shown in the inset. The main panel shows the SOT-switching signal where V_{DC2} in the magnetization direction along $+y$ was set to 0 μV for easy analysis. The arrows indicate the sweep direction of J_{PLS}. (c) ΔV as a function of J_{PLS} at $\theta_H = 0°$. Steps (1)–(3) were carried out only before starting the measurements. The arrows indicate the sweep direction of J_{PLS}. (d), (e) ΔV as a function of J_{PLS} at various values of (d) f_{MW} and (e) the pulse width W_{PLS} at $\theta_H = 0°$. (f) ΔV and (g) normalized ΔV as functions of J_{PLS} for $L_x = 500$ nm, 2 μm, 4 μm, and 20 μm. The inset of (f) shows the magnitude of the SOT-switching signal as a function of L_x.

20 μm, 200 MHz, and 10 dBm, respectively. B_{SET} was +300 (–300) mT for the up (down) J_{PLS} sweep, indicating that the initial magnetization direction was $+y$ $(-y)$ for the up (down) sweep. The arrows indicate the sweep direction of J_{PLS}. Steps (1)–(6) were all repeated for each measurement. In Fig. 5, B_{PLS} was precisely adjusted to 0 mT by monitoring the Hall device. The pulse width of W_{PLS} was 1 ms. Because ΔV is defined as the difference $V_{DC2} - V_{DC1}$, the raw $\Delta V - J_{PLS}$ curve does not show the typical hysteresis of SOT switching, as shown in the inset of Fig. 5(b). Therefore, as shown in the main panel of Fig. 5(b), V_{DC2} in the magnetization direction along $+y$ was set to 0 μV for easy analysis. A clear hysteresis with steep change ΔV around $J_{PLS} = \pm 15\,\text{MA/cm}^2$ was observed, a typical feature of SOT magnetization switching. The magnitude of the hysteresis was 600 nV, comparable to ΔV_0 in Fig. 4. Next, we skipped the optional steps (1)–(2), i.e., positive (negative) B_{SET} was applied once before starting the up (down) sweep measurements. A similar hysteresis was obtained as shown in Fig. 5(c).

Hereafter, we show the $\Delta V - J_{PLS}$ curves only for the up sweep because those of the down sweep are the same in the following discussions. Figure 5(d) shows the $\Delta V - J_{PLS}$ curve for various f_{MW} values at $\theta_H = 0°$. Whereas the $\Delta V - J_{PLS}$ curve shows almost the same behavior for $10\,\text{MHz} \leqslant f_{MW} \leqslant 200\,\text{MHz}$, its magnitude gradually decreases with increasing f_{MW} and is almost zero above 2 GHz, in agreement with the LFST-FMR signals in Figs. 3(a) and 4. $\Delta V - J_{PLS}$ curves for various pulse widths W_{PLS} are shown in Fig. 5(e). The threshold value of J_{PLS} was $10\,\text{MA/cm}^2$ for $W_{PLS} \geqslant 500\,\mu$s, and it increased with decreasing W_{PLS}. Several step-like shapes also appear during the magnetization switching. Because L_y was 20 μm, which was considerably long compared with L_x, domain-wall propagation along the y direction is expected to be dominant in the magnetization switching process. In this situation, the shape of the $\Delta V - J_{PLS}$ curves strongly depends on the velocity of the domain-wall propagation. Assuming a typical domain-wall velocity of the Py layer ($v < 100$ m/s), at least 200 ns is needed to propagate the domain wall through the 20-μm-long Py layer [50–52]. The heat effect also contributes to modulating the $\Delta V - J_{PLS}$ curves [53,54]. To evaluate the SOT switching time accurately, L_y should be decreased to a practical device size. Figures 5(f) and 5(g) show the L_x dependence of the $\Delta V - J_{PLS}$ curves and the normalized ones. The magnitude of the $\Delta V - J_{PLS}$ curves as a function of L_x is shown in the inset of Fig. 5(f). Whereas a linear relationship between signal magnitude and L_x is recognized below $L_x = 4\,\mu$m, that of 20 μm was deviated from the trend. Because $L_x = 20$-μm sample has a square-shape Py electrode, magnetization direction no longer aligns along the y direction at $B_{ext} = 0$ mT resulting in a reduction in the signal magnitude. The switching feature was made steeper by decreasing L_x because of the complicated domain structure and domain-wall motion for large L_x.

V. MICROMAGNETIC SIMULATION OF ST-FMR AND FIELD-INDUCED FMR

In this section, we discuss the possible origin of the obtained DC voltage in LFST-FMR. There are several differences in conditions between LFST-FMR and typical ST-FMR measurements. First, B_{ext} was 0 mT during the FMR measurements in LFST-FMR. Therefore, the magnetization is expected to align along the y direction owing to the shape anisotropy. Second, the microwave frequency was sub-GHz, one or two orders smaller than typical frequencies. Third, the AC magnetic field was along the y direction, parallel to the magnetization direction. V_{DC} due to the spin rectification

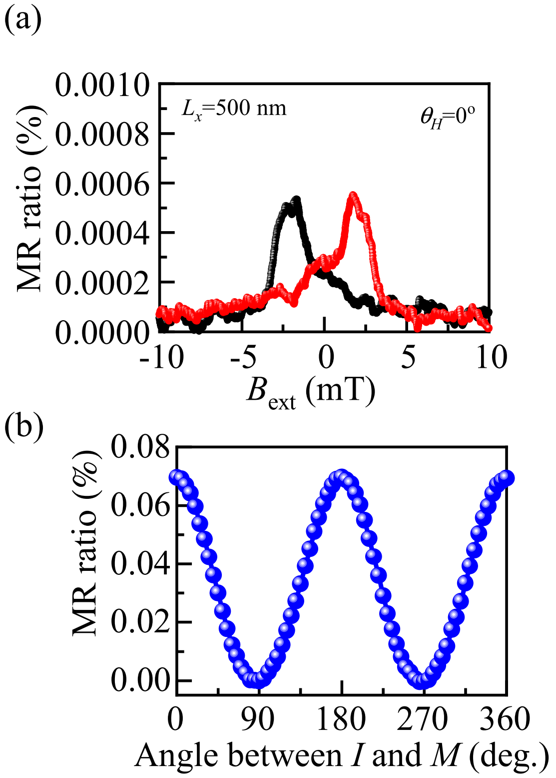

FIG. 6. (a) AMR ratio as a function of B_{ext} for the Py/Pt device, obtained from two terminal resistances between the signal line and ground line in Fig. 1(b). (b) AMR ratio as a function of angle between direct current I and magnetization M for the Py/Pt films. The AMR ratio was calculated from the four terminal resistances.

effect is

$$V_{\text{DC}} = \left\langle I_{\text{MW}} \sin(2\pi f_{\text{MW}} t)\, B_{\text{MW}} \frac{dR}{dB_{\text{ext}}} \sin(2\pi f_{\text{MW}} t - \varphi) \right\rangle, \quad (3)$$

where ⟨⟩ denotes the time average, φ is the phase difference between M and alternating current in the Py/Pt device, t is the time, and B_{MW} is the magnetic flux density generated by the microwave. $\frac{dR}{dB_{\text{ext}}}$ is generally expected to be negligible at $\theta_H = 0°$ because B_{MW} is parallel to the magnetization direction and the precession axis is along the y direction. However, the magnitude of the LFST-FMR in Fig. 3 is unexpectedly comparable to or higher than that of the typical ST-FMR in Figs. 1 and 2. To find the origin of such a large signal, we first measured the magnetoresistance (MR) of the device by applying B_{ext} at $\theta_H = 0°$ and a direct current of 1 mA. Figure 6(a) shows the MR ratio as a function of B_{ext}. A direct current was applied along the $+x$ direction. Triangular hysteresis signals were obtained with a switching field of $B_{\text{ext}} = 3$ mT, a typical shape for anisotropic magnetoresistance (AMR) with an external magnetic field along the magnetic easy axis. We also measured the MR ratio as a function of θ_H for the Py/Pt bilayer without device fabrication to investigate the AMR magnitude in the Py/Pt bilayer structure. The applied magnetic field was 100 mT, sufficiently high to align the magnetization along B_{ext}. Whereas a clear sine shape was obtained as shown in Fig. 6(b), the MR ratio was only 0.07%, approximately one order of magnitude smaller than that of typical Py, owing to the considerable parallel conduction of the Pt layer. In practical devices, the MR ratio is much smaller than that in Fig. 6(b) because the parasitic resistance of the Pt leads connected in series to the Py/Pt bilayer electrodes is dominant. Here we note that a finite $\frac{dR}{dB_{\text{ext}}}$ was obtained at 0 mT as shown in Fig. 6(a), which might be due to the tilt of the magnetization especially at edge areas (see the Supplemental Material [47]). $\frac{dR}{dB_{\text{ext}}}$ around 0 ± 0.5 mT was +27 ± 2 and −53 ± 2 mΩ/T for the up and down sweep, respectively. The nonzero $\frac{dR}{dB_{\text{ext}}}$ around 0 mT indicates that the resistance of the sample actually changes even for application of low B_{MW} along the y axis. B_{MW} is estimated to be 0.43 mT at 10 dBm, which yields a resistance change of 3.7×10^{-5} Ω.

From the micromagnetic simulation, the magnetic resonance frequency is calculated to be 1.425 GHz at 0 mT (see Supplemental Material [47]). For $f_{\text{MW}} \leqslant 1$ GHz, φ due to the SOT and Oersted field is expected to be 90° and 0°, respectively. In this case, ΔV_0 at $B_{\text{ext}} = 0$ mT and $\theta_H = 0°$ due to the Oersted field is simply expressed as

$$\Delta V_0 = I_{\text{MW}} B_{\text{MW}} \frac{dR}{dB_{\text{ext}}}.$$

Because we measured $\frac{dR}{dB_{\text{ext}}}$ for the whole Py/Pt bilayer, we used an alternating current in the whole Py/Pt layer, I_{MW}. Using $I_{\text{MW}} = 1.8 \times 10^{-2}$ A, $B_{\text{MW}} = 0.43$ mT, and $\frac{dR}{dB_{\text{ext}}} = 40$ mΩ/T, ΔV_0 is calculated to be 310 nV, approximately half of the experimental value in Fig. 4. The difference between experimental and theoretical ΔV_0 might be due to the contribution of ferromagnetic resonance. Whereas the ferromagnetic resonance frequency at 0 mT was around 1.425 GHz (see Supplemental Material [47]), it has a finite dispersion according to location in the Py layer. Therefore, several parts of the Py electrode match the ferromagnetic condition, resulting in an enhancement of $\frac{dR}{dB_{\text{ext}}}$ [55]. In this case, φ changes from 0°, and an SOT contribution to ΔV_0 is expected.

V_{DC} can also be generated by the anomalous Nernst effect (ANE) and by the combination of spin pumping and the ISHE. For the ANE, the temperature gradient along the z direction due to microwave absorption thermally activates carriers that flow along the z direction and generate an electric field along the x direction. The ANE-DC voltage V_{ANE} is

$$V_{\text{ANE}} = \alpha_{\text{N}} \frac{L_x \Delta T_{\text{Py}}}{t_{\text{Py}}},$$

where $\alpha_{\text{N}} = 4.8$ nV/K is the ANE coefficient of Py, and ΔT_{Py} is the temperature difference between the top and bottom surfaces of the Py layer [56]. ΔT_{Py} is generally less than several tens of mK at maximum because the Py layer is very thin. Assuming $\Delta T_{\text{Py}} = 10$ mK, V_{ANE} is expected to be at maximum 6 nV in this study, which is negligible. For the combination of spin pumping and the ISHE, magnetic precession of the Py layer generates a pure spin current J_s along the z direction, and J_s is converted into a charge current via the ISHE. Assuming the typical mixing conductance in Py/Pt interfaces, $g_r^{\uparrow\downarrow} = 2.31 \times 10^{19}\ \text{m}^{-2}$, the spin current generated by spin pumping is estimated to be $J_s = 1.7 \times 10^{-14}\ \text{J/m}^2$ [57,58]. Using the typical spin Hall angle, $\theta_{\text{SHE}} = 0.04$, and spin-diffusion length of 10 nm, the DC voltage generated by the ISHE is estimated to be 2.4×10^{-13} V, also negligible

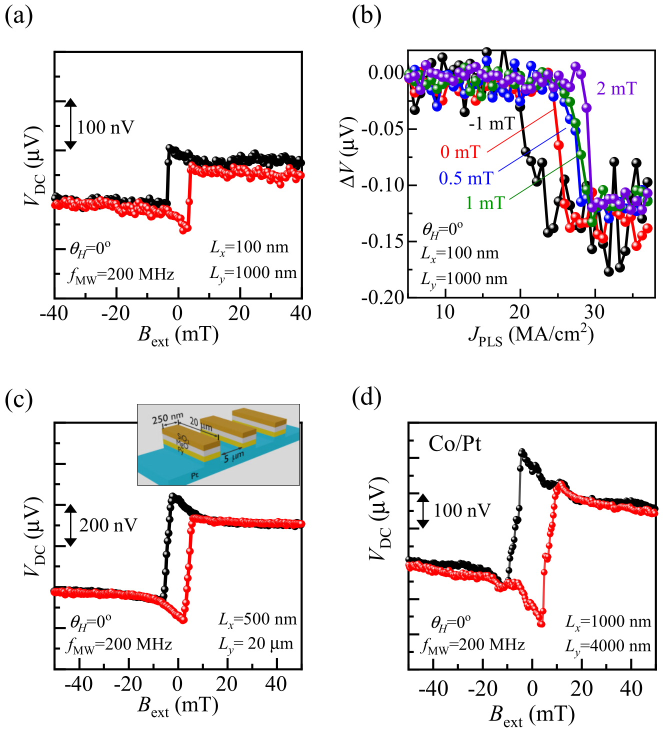

FIG. 7. (a) $V_{DC} - B_{ext}$ curve for the Py electrode with $L_x =$ 100 nm and $L_y = 1000$ nm at $\theta_H = 0^\circ$. f_{MW} and P_{MW} were 200 MHz and 5 dBm, respectively. (b) ΔV as a function of J_{PLS} at various B_{PLS} values with $W_{PLS} = 1\,\mu$s. (c) V_{DC}–B_{ext} curve for the three Py electrodes in series on a Pt layer. The edge-to-edge distance between the Adjacent Py electrodes were 5 μm. L_x, L_y, f_{MW}, and P_{MW} were 500 nm, 20 μm, 200 MHz, and 10 dBm, respectively. (d) $V_{DC} - B_{ext}$ curve for the 4-nm-thick Co electrode with $L_x = 1000$ nm and $L_y =$ 4000 nm at $\theta_H = 0^\circ$. f_{MW} and P_{MW} were 200 MHz and 5 dBm, respectively.

compared with ΔV_0 in Fig. 4 (see Supplemental Material [47]).

VI. APPLICATION TO A PRACTICAL DEVICE WITH A SMALL FERROMAGNET

The typical device of a practical MTJ has a diameter of less than 100 nm, which is one order of magnitude smaller than that of our device. Furthermore, Py is not a suitable ferromagnetic material for a high MR ratio in an MTJ. Therefore, we now discuss the possibility of applying LFST-FMR to the small ferromagnetic electrode of a practical device. We first fabricated a sample with $L_x = 100$ nm and $L_y = 1000$ nm. The LFST-FMR signal is shown in Fig. 7(a). Because V_{DC} depends not on L_y but on L_x, a decrease in L_y is possible without significant reduction in V_{DC}. We determined L_y for impedance matching and sufficient shape anisotropy. P_{MW} and W_{PLS} were 5 dBm and 1 μs, respectively, because of the smaller device size. A clear rectangular signal was still detected in the $V_{DC} - B_{ext}$ curve as shown in Fig. 7(a). ΔV_0 at 0 mT is around 0.15 μV, approximately one-fourth that of the $L_x =$ 500-nm sample in Fig. 3. Figure 7(b) shows $\Delta V - J_{PLS}$ curves for the $L_x =$ 100-nm device. A varying static magnetic field B_{PLS} was applied during the pulse voltage [see step (3) in Fig. 5(a)] to investigate contributions of the SOT and Oersted field to magnetization switching. Positive (negative) B_{PLS} corresponds to a magnetic field that impedes (assists) the magnetization switching. For $B_{PLS} = 0$ mT, a steep change in ΔV is obtained at 25 MA/cm^2. The switching feature was steeper than in Fig. 5 because L_y, which determines the length of the domain-wall propagation, was decreased by a factor of 20. Whereas the Oersted field from J_{PLS} is estimated to be less than 1–2 mT, successful switching was obtained even for $B_{PLS} = 2$ mT, indicating a non-negligible SOT contribution.

We also propose an enhancement of signal amplitude and a statistical investigation of the magnetization switching characteristics by fabricating several Py electrodes in series on a Pt layer. An increased number of ferromagnetic electrodes is expected to contribute an increase in V_{DC}, which enables downsizing of the ferromagnetic electrodes. Figure 7(c) displays an LFST-FMR signal for a device equipped with three ferromagnetic electrodes with $L_x = 500$ nm. Clear hysteresis was obtained with $\Delta V_0 = 500$ nV ($P_{MW} = 10$ dBm). Because the length of the Pt lead was increased by increasing the number of Py electrodes in this device, ΔV_0 does not show a linear relationship with the number of Py electrodes. Optimization of the Pt lead structure is desired.

To confirm the applicability of LFST-FMR to other ferromagnetic materials, we fabricated a device with a Co electrode on Pt films. The AMR magnitude of Co is much smaller than that in a Py layer [59,60]. We obtained clear rectangular signals even for the Co electrode as shown in Fig. 7(c). The magnitude of ΔV_0 depends on the charge-current density in the ferromagnetic layer and magnitude of $\frac{dR}{dB_{ext}}$. Whereas low $\frac{dR}{dB_{ext}}$ is expected owing to the low AMR, the charge-current density in the Co layer is expected to increase owing to the low resistivity of the Co layer compared with that of the Py electrode, resulting in considerable ΔV_0. Because we used a relatively thick Pt layer (15 nm), further enhancement of ΔV_0 is possible by decreasing the thickness of the Pt layer. The coercive force of ferromagnetic electrodes in a practical device is expected to be greater than that of a Py electrode. In that case, magnetization motion around 0 mT might be strongly suppressed, resulting in the reduction in $\frac{dR}{dB_{ext}}$. Under the absence of AMR signal around 0 mT due to a strong magnetic anisotropy, considerably small $\frac{dR}{dB_{ext}}$ is expected, which is generated by the magnon magnetoresistance (MMR) [61,62]. The magnitude of $\frac{dR}{dB_{ext}}$ due to the MMR is generally several mΩ/T, an order of magnitude smaller than that obtained in this study. Even in this case, LFST-FMR can be applied using a finite magnetic field during FMR measurements as long as the $R - B_{ext}$ curve shows hysteresis behavior. When magnetic field is applied, the magnetization starts to tilt from the y axis only when the magnetic field is antiparallel to the magnetization direction. In this situation, a different $\frac{dR}{dB_{ext}}$ value is obtained for $M// + y$ and $M//{-y}$.

VII. CONTRIBUTIONS OF THE SOT AND OERSTED FIELD IN THE MAGNETIZATION SWITCHING AND LFST-FMR

Finally, we briefly discuss the contributions of SOT and Oersted field in the magnetization switching and LFST-FMR. We need to discuss separately the mechanisms of magnetization switching and generation of DC voltage in LFST-FMR. In the former case, there are two contributions for the magnetization switching, i.e., the spin-orbit torque and the Oersted field. Because the magnetization switching was successfully demonstrated even though the Oersted field was canceled out by additional magnetic field as shown in Fig. 7(b), we concluded that there was non-negligible contribution from SOT. It is noted that the threshold of J_{PLS} was actually increased from $\sim$25 to 30 $\mathrm{MA/cm^2}$ by applying $B_{\mathrm{PLS}} = 2$ mT, indicating that the Oersted field also contributes the magnetization switching. On the basis of a simple assumption, the SOT is dominant because the increment of J_{PLS} due to the cancellation of the Oersted field is just 20%. However, the difference in magnetization direction before application of J_{PLS} between $B_{\mathrm{PLS}} = 0$ and 2 mT should be considered for the accurate evaluation of the SOT contribution. According to above discussion, we expect that both SOT and Oersted field contribute to the magnetization motion in the LFST-FMR, where not a pulse current but an AC current is applied. Here, we should consider the phase difference φ between the AC charge current in the Py layer and the magnetization motion as shown in Eq. (3). Because the DC voltage has a linear relationship with $\cos\varphi$, DC voltage generated by the Oersted field at the ferromagnetic resonant condition ($\varphi = 90^\circ$), is estimated to be 0 V. Therefore, the suitable condition for generation of DC voltage is below the resonant frequency, where the considerable magnetic susceptibility is also expected. Note that the magnetic susceptibility reaches 0 above the resonant frequency (see Supplemental Material [47]). In contrast, because the DC voltage generated by the dampinglike torque of the SOT has a linear relationship with $\sin\varphi$, the resonant condition is suitable. Therefore, while the dominant contribution of SOT switching is expected to be the dampinglike SOT, that of DC voltage generation in LFST-FMR is expected to be the Oersted field and/or the fieldlike SOT.

VIII. CONCLUSION

We have demonstrated in-plane magnetization switching of a permalloy/platinum bilayer induced by SOT using the spin rectification effect with sub-GHz microwaves. Because the magnitude of the LFST-FMR signal is the same or larger than that of a typical ST-FMR signal, a highly sensitive detection of magnetization switching has been realized in spite of deviation from the optimal ST-FMR condition. The proposed method is applicable to a simple device structure even for a ferromagnetic electrode as small as 100 nm wide.

ACKNOWLEDGMENT

This work was supported by JSPS (KAKENHI No. 16H06330, No. 19H02197 and No. 20H02607).

---

[1] I. M. Miron, K. Garello, G. Gaudin, P. J. Zermatten, M. V. Costache, S. Auffret, S. Bandiera, B. Rodmacq, A. Schuhl, and P. Gambardella, Nature (London) **476**, 189 (2011).

[2] L. Liu, C.-F. Pai, Y. Li, H. W. Tseng, D. C. Ralph, and R. A. Buhrman, Science **336**, 555 (2012).

[3] L. Liu, O. J. Lee, T. J. Gudmundsen, D. C. Ralph, and R. A. Buhrman, Phys. Rev. Lett. **109**, 096602 (2012).

[4] K. Garello, I. M. Miron, C. O. Avci, F. Freimuth, Y. Mokrousov, S. Blügel, S. Auffret, O. Boulle, G. Gaudin, and P. Gambardella, Nat. Nanotechnol. **8**, 587 (2013).

[5] G. Yu, P. Upadhyaya, Y. Fan, J. G. Alzate, W. Jiang, K. L. Wong, S. Takei, S. A. Bender, L. Te Chang, Y. Jiang, M. Lang, J. Tang, Y. Wang, Y. Tserkovnyak, P. K. Amiri, and K. L. Wang, Nat. Nanotechnol. **9**, 548 (2014).

[6] K. Garello, C. O. Avci, I. M. Miron, M. Baumgartner, A. Ghosh, S. Auffret, O. Boulle, G. Gaudin, and P. Gambardella, Appl. Phys. Lett. **105**, 212402 (2014).

[7] S. Fukami, T. Anekawa, C. Zhang, and H. Ohno, Nat. Nanotechnol. **11**, 621 (2016).

[8] S. O. Valenzuela and M. Tinkham, Nature (London) **442**, 176 (2006).

[9] T. Kimura, Y. Otani, T. Sato, S. Takahashi, and S. Maekawa, Phys. Rev. Lett. **98**, 156601 (2007).

[10] T. Seki, Y. Hasegawa, S. Mitani, S. Takahashi, H. Imamura, S. Maekawa, J. Nitta, and K. Takanashi, Nat. Mater. **7**, 125 (2008).

[11] Y. Niimi, Y. Kawanishi, D. H. Wei, C. Deranlot, H. X. Yang, M. Chshiev, T. Valet, A. Fert, and Y. Otani, Phys. Rev. Lett. **109**, 156602 (2012).

[12] H. L. Wang, C. H. Du, Y. Pu, R. Adur, P. C. Hammel, and F. Y. Yang, Phys. Rev. Lett. **112**, 197201 (2014).

[13] H. An, Y. Kageyama, Y. Kanno, N. Enishi, and K. Ando, Nat. Commun. **7**, 13069 (2016).

[14] Y.-C. Lau, H. Lee, G. Qu, K. Nakamura, and M. Hayashi, Phys. Rev. B **99**, 064410 (2019).

[15] K. Ando, S. Takahashi, J. Ieda, H. Kurebayashi, T. Trypiniotis, C. H. W. Barnes, S. Maekawa, and E. Saitoh, Nat. Mater. **10**, 655 (2011).

[16] K. Ando and E. Saitoh, Nat. Commun. **3**, 629 (2012).

[17] M. Koike, E. Shikoh, Y. Ando, T. Shinjo, S. Yamada, K. Hamaya, and M. Shiraishi, Appl. Phys. Express **6**, 023001 (2013).

[18] A. Yamamoto, Y. Ando, T. Shinjo, T. Uemura, and M. Shiraishi, Phys. Rev. B **91**, 024417 (2015).

[19] A. R. Mellnik, J. S. Lee, A. Richardella, J. L. Grab, P. J. Mintun, M. H. Fischer, A. Vaezi, A. Manchon, E. A. Kim, N. Samarth, and D. C. Ralph, Nature (London) **511**, 449 (2014).

[20] Y. Shiomi, K. Nomura, Y. Kajiwara, K. Eto, M. Novak, K. Segawa, Y. Ando, and E. Saitoh, Phys. Rev. Lett. **113**, 196601 (2014).

[21] Y. Ando, T. Hamasaki, T. Kurokawa, K. Ichiba, F. Yang, M. Novak, S. Sasaki, K. Segawa, Y. Ando, and M. Shiraishi, Nano Lett. **14**, 6226 (2014).

[22] Y. Fan, P. Upadhyaya, X. Kou, M. Lang, S. Takei, Z. Wang, J. Tang, L. He, L. Te Chang, M. Montazeri, G. Yu, W. Jiang, T. Nie, R. N. Schwartz, Y. Tserkovnyak, and K. L. Wang, Nat. Mater. **13**, 699 (2014).

[23] Y. Fan, X. Kou, P. Upadhyaya, Q. Shao, L. Pan, M. Lang, X. Che, J. Tang, M. Montazeri, K. Murata, L. Te Chang, M. Akyol, G. Yu, T. Nie, K. L. Wong, J. Liu, Y. Wang, Y. Tserkovnyak, and K. L. Wang, Nat. Nanotechnol. **11**, 352 (2016).
[24] K. Kondou, R. Yoshimi, A. Tsukazaki, Y. Fukuma, J. Matsuno, K. S. Takahashi, M. Kawasaki, Y. Tokura, and Y. Otani, Nat. Phys. **12**, 1027 (2016).
[25] Y. Ando and M. Shiraishi, J. Phys. Soc. Jpn. **86**, 011001 (2017).
[26] N. H. D. Khang, Y. Ueda, and P. N. Hai, Nat. Mater. **17**, 808 (2018).
[27] Y. Liu, J. Besbas, Y. Wang, P. He, M. Chen, D. Zhu, Y. Wu, J. M. Lee, L. Wang, J. Moon, N. Koirala, S. Oh, and H. Yang, Nat. Commun. **9**, 2492 (2018).
[28] Z. Chi, Y.-C. Lau, X. Xu, T. Ohkubo, K. Hono, and M. Hayashi, Sci. Adv. **6**, eaay2324 (2020).
[29] K. Ando, S. Watanabe, S. Mooser, E. Saitoh, and H. Sirringhaus, Nat. Mater. **12**, 622 (2013).
[30] R. Ohshima, A. Sakai, Y. Ando, T. Shinjo, K. Kawahara, H. Ago, and M. Shiraishi, Appl. Phys. Lett. **105**, 162410 (2014).
[31] J. B. S. Mendes, O. Alves Santos, L. M. Meireles, R. G. Lacerda, L. H. Vilela-Leão, F. L. A. Machado, R. L. Rodríguez-Suárez, A. Azevedo, and S. M. Rezende, Phys. Rev. Lett. **115**, 226601 (2015).
[32] S. Dushenko, H. Ago, K. Kawahara, T. Tsuda, S. Kuwabata, T. Takenobu, T. Shinjo, Y. Ando, and M. Shiraishi, Phys. Rev. Lett. **116**, 166102 (2016).
[33] L. Liu, T. Moriyama, D. C. Ralph, and R. A. Buhrman, Phys. Rev. Lett. **106**, 036601 (2011).
[34] M. Harder, Z. X. Cao, Y. S. Gui, X. L. Fan, and C.-M. Hu, Phys. Rev. B **84**, 054423 (2011).
[35] M. Harder, Y. Gui, and C.-M. Hu, Phys. Rep. **661**, 1 (2016).
[36] A. Wirthmann, X. Fan, Y. S. Gui, K. Martens, G. Williams, J. Dietrich, G. E. Bridges, and C.-M. Hu, Phys. Rev. Lett. **105**, 017202 (2010).
[37] Y. Zhang, Q. Liu, B. F. Miao, H. F. Ding, and X. R. Wang, Phys. Rev. B **99**, 064424 (2019).
[38] U. Chaudhuri, R. Mahendiran, and A. O. Adeyeye, Appl. Phys. Lett. **115**, 022406 (2019).
[39] E. Saitoh, M. Ueda, H. Miyajima, and G. Tatara, Appl. Phys. Lett. **88**, 182509 (2006).
[40] K. Kondou, H. Sukegawa, S. Kasai, S. Mitani, Y. Niimi, and Y. Otani, Appl. Phys. Express **9**, 023002 (2016).
[41] Y. Huo, F. L. Zeng, C. Zhou, and Y. Z. Wu, Phys. Rev. Appl. **8**, 014022 (2017).
[42] S. Yoon, J. Liu, and R. D. McMichael, Phys. Rev. B **93**, 144423 (2016).
[43] C. Kim, D. Kim, B. S. Chun, K.-W. Moon, and C. Hwang, Phys. Rev. Appl. **9**, 054035 (2018).
[44] C.-F. Pai, L. Liu, Y. Li, H. W. Tseng, D. C. Ralph, and R. A. Buhrman, Appl. Phys. Lett. **101**, 122404 (2012).
[45] S. V. Aradhya, G. E. Rowlands, J. Oh, D. C. Ralph, and R. A. Buhrman, Nano Lett. **16**, 5987 (2016).
[46] Y. Wang, D. Zhu, Y. Wu, Y. Yang, J. Yu, R. Ramaswamy, R. Mishra, S. Shi, M. Elyasi, K.-L. Teo, Y. Wu, and H. Yang, Nat. Commun. **8**, 1364 (2017).
[47] See Supplemental Material at http://link.aps.org/supplemental/10.1103/PhysRevB.102.174442 for more details on the device fabrication procedures and micromagnetic simulation.
[48] X. F. Zhu, M. Harder, J. Tayler, A. Wirthmann, B. Zhang, W. Lu, Y. S. Gui, and C.-M. Hu, Phys. Rev. B **83**, 140402(R) (2011).
[49] L. Pan, W. T. Soh, N. N. Phuoc, and C. K. Ong, Phys. Status Solidi (RRL) **12**, 1800178 (2018).
[50] A. Yamaguchi, T. Ono, S. Nasu, K. Miyake, K. Mibu, and T. Shinjo, Phys. Rev. Lett. **92**, 077205 (2004).
[51] M. Hayashi, L. Thomas, Y. B. Bazaliy, C. Rettner, R. Moriya, X. Jiang, and S. S. P. Parkin, Phys. Rev. Lett. **96**, 197207 (2006).
[52] M. Hayashi, L. Thomas, C. Rettner, R. Moriya, Y. B. Bazaliy, and S. S. P. Parkin, Phys. Rev. Lett. **98**, 037204 (2007).
[53] E. B. Myers, F. J. Albert, J. C. Sankey, E. Bonet, R. A. Buhrman, and D. C. Ralph, Phys. Rev. Lett. **89**, 196801 (2002).
[54] R. Lo Conte, A. Hrabec, A. P. Mihai, T. Schulz, S.-J. Noh, C. H. Marrows, T. A. Moore, and M. Kläui, Appl. Phys. Lett. **105**, 122404 (2014).
[55] T. Moriyama, R. Cao, J. Q. Xiao, J. Lu, X. R. Wang, Q. Wen, and H. W. Zhang, Appl. Phys. Lett. **90**, 152503 (2007).
[56] J. Holanda, O. Alves Santos, R. O. Cunha, J. B. S. Mendes, R. L. Rodríguez-Suárez, A. Azevedo, and S. M. Rezende, Phys. Rev. B **95**, 214421 (2017).
[57] K. Ando and E. Saitoh, J. Appl. Phys. **108**, 113925 (2010).
[58] K. Ando, S. Takahashi, J. Ieda, Y. Kajiwara, H. Nakayama, T. Yoshino, K. Harii, Y. Fujikawa, M. Matsuo, S. Maekawa, and E. Saitoh, J. Appl. Phys. **109**, 103913 (2011).
[59] T. R. Mcguire and R. I. Potter, IEEE Trans. Magn. **11**, 1018 (1975).
[60] W. Gil, D. Görlitz, M. Horisberger, and J. Kötzler, Phys. Rev. B **72**, 134401 (2005).
[61] A. P. Mihai, J. P. Attané, A. Marty, P. Warin, and Y. Samson, Phys. Rev. B **77**, 060401(R) (2008).
[62] V. D. Nguyen, P. Laczkowski, A. Marty, L. Notin, C. Beigné, L. Vila, and J. P. Attané, J. Appl. Phys. **115**, 053912 (2014).